

# Efficient Simulation of Chemical–Mechanical Coupling in Battery Active Particles

Giuseppe F. Castelli,\* Lars von Kolzenberg,\* Birger Horstmann, Arnulf Latz, and Willy Dörfler

Coupling of chemistry and mechanics causes large stresses and deterioration in battery active particles, which undergo a phase change. The Cahn–Hilliard approach coupled to large deformations provides a framework to theoretically investigate the underlying physics. However, solving this model is computationally expensive, so that the current application is limited. In this article, a thermodynamically consistent phase-field model coupling Cahn–Hilliard-type phase separation and large deformations is developed. The model is implemented using a space and time adaptive numerical solution algorithm based on the finite element method. At the example of lithium iron phosphate, simulations are performed to investigate physical and numerical aspects of the model and the solver. The strong interrelation between chemistry, phase transformation, and mechanics is shown. In particular, the interfacial energy coefficient has a major impact on the stress inside the material. Moreover, the presented solution algorithm outperforms classical implementations. This enables the analysis of computationally demanding parameter choices and multidimensional geometries.

## 1. Introduction

The decarbonization of society requires efficient storage of energy for portable, mobile, and stationary applications, e.g., stabilization of power grids based on fluctuating renewable energy sources. A promising approach for this challenge are electrochemical storage systems in the form of batteries. For mobile applications, lithium-ion batteries are the state-of-the-art technology as they comprise high energy density and good cyclability.<sup>[1]</sup> Improving the performance of lithium-ion batteries is, thus, key toward a green future.

A critical issue limiting the performance and lifetime of lithium-ion batteries is the coupling of chemistry and mechanics inside the battery active particles. The lithium uptake of the host material leads to volume mismatch inside the particles. This causes mechanical stress, which eventually leads to particle fracture and thereby capacity loss.<sup>[2,3]</sup> In turn, the mechanical stress influences the diffusion of lithium inside the host.<sup>[2,4–7]</sup> These effects are especially pronounced for phase separating materials, e.g., lithium manganese oxide spinel  $\text{Li}_x\text{Mn}_2\text{O}_4$  (LMO), lithium iron phosphate  $\text{Li}_x\text{FePO}_4$  (LFP) and group IV elements (silicon, germanium, and tin), which form a lithium poor and a lithium rich phase during battery operation.<sup>[8–14]</sup>

Physical models extend our understanding of the chemical–mechanical coupling and the phase separation within the electrode particles. The Cahn–Hilliard theory<sup>[15,16]</sup> provides a framework to consistently describe diffusion and phase separation based on a free energy functional. By extending this free energy functional for mechanical contributions, a consistent description of the chemical–mechanical coupling emerges. Several groups implemented these models to describe the lithiation of silicon,<sup>[17–20]</sup>  $\text{Li}_x\text{Mn}_2\text{O}_4$ ,<sup>[11,21–23]</sup>  $\text{Li}_x\text{FePO}_4$ ,<sup>[23–30]</sup> or the sodiation of  $\text{Na}_x\text{FePO}_4$ .<sup>[23–25]</sup>


However, phase-field models are computationally demanding, which impedes their application in simulations of full cells. The geometric nonlinearity of large deformations and the higher order differential operators impose a numerical challenge. In addition, the quasi-instantaneous formation and comparable slow migration of an almost sharp phase transition causes a strong variation of the spatial and temporal scales. Thus, the accurate solution of the model equations requires a high spatial and temporal resolution and many large linear systems to solve.

G. F. Castelli, Prof. W. Dörfler  
Institute of Applied and Numerical Mathematics  
Karlsruhe Institute of Technology (KIT)  
Englerstr. 2, 76131 Karlsruhe, Germany  
E-mail: fabian.castelli@kit.edu

L. von Kolzenberg, Dr. B. Horstmann, Prof. A. Latz  
Institute of Engineering Thermodynamics  
German Aerospace Center (DLR)  
Pfaffenwaldring 38–40, 70569 Stuttgart, Germany  
E-mail: lars.kolzenberg@dlr.de

L. von Kolzenberg, Dr. B. Horstmann, Prof. A. Latz  
Helmholtz Institute Ulm (HIU)  
Helmholtzstr. 11, 89081 Ulm, Germany

Dr. B. Horstmann, Prof. A. Latz  
Institute of Electrochemistry  
Ulm University (UUI)  
Albert-Einstein-Allee 47, 89081 Ulm, Germany

 The ORCID identification number(s) for the author(s) of this article can be found under <https://doi.org/10.1002/ente.202000835>.

© 2021 The Authors. Energy Technology published by Wiley-VCH GmbH. This is an open access article under the terms of the Creative Commons Attribution-NonCommercial License, which permits use, distribution and reproduction in any medium, provided the original work is properly cited and is not used for commercial purposes.

DOI: 10.1002/ente.202000835

In literature, similar phase-field models coupling chemical–mechanical intercalation processes were already discussed.<sup>[11,17–19,21–26,30–34]</sup> To overcome the numerical challenge caused by the higher order differential operators, oftentimes a mixed formulation was considered, introducing a new solution variable and splitting the equations into two second-order equations.<sup>[11,17–19,21–26,30,31]</sup> In contrast, Xu and co-workers<sup>[32–34]</sup> treated the fourth-order derivative straightforward using the isogeometric analysis. However, only marginally advanced numerical techniques such as adaptivity were used to overcome the heterogeneities in spatial and temporal scale.<sup>[25]</sup>

In this article, we develop a phase-field model for phase separating electrode materials coupling chemistry, mechanics, and phase separation consistently with a common free energy functional. We consider a mixed formulation of the model equations and present a convergent, space and time adaptive, higher order finite element solver with a fully implicit, variable-step, variable-order time integration scheme. Due to the adaptive solution algorithm, we create large computational savings, which allows us to perform numerical experiments in crucial parameter regimes efficiently.

The rest of this article is organized as follows: Next in Section 2, we derive our model to describe phase transformation and chemical–mechanical coupling during battery operation. Following, we explain our numerical solution algorithm in Section 3. We discuss the simulation results of this methodology in Section 4 and summarize the key findings in Section 5.

## 2. Model Development

In this section, we derive a phase-field model to describe the chemical–mechanical coupling in phase transforming materials. First, we model the chemical and mechanical deformation of the electrode particle. Afterwards, we state a phase-field model accounting for the phase separation of the material. From this phase-field model, we consistently derive equations to describe mechanics and chemistry in the last two subsections.

### 2.1. Deformation

During battery operation, the particle deforms from its initial (reference) configuration  $\Omega_0$  to the current configuration  $\Omega$ , as shown in **Figure 1**. We describe this process with the deformation gradient  $\mathbf{F} = \partial \mathbf{x} / \partial \mathbf{X}_0$ , which corresponds to the mapping of a point  $\mathbf{X}_0$  from the reference configuration to a point  $\mathbf{x}$  in the

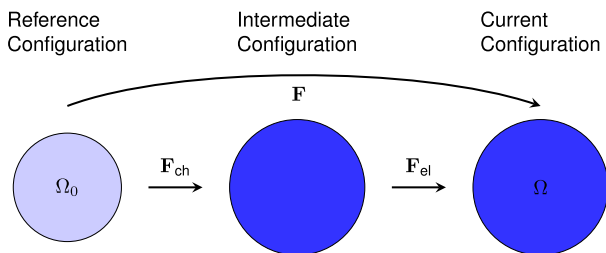


**Figure 1.** The particle first deforms chemically  $\mathbf{F}_{\text{ch}}$  then elastically  $\mathbf{F}_{\text{el}}$ , leading to the overall deformation  $\mathbf{F}$ .

current configuration. The displacement  $\mathbf{u}$  is incorporated in this mapping according to

$$\mathbf{F} = \mathbf{Id} + \nabla \mathbf{u} \quad (1)$$

with the identity matrix  $\mathbf{Id}$ .<sup>[35,36]</sup> We multiplicatively split the deformation according to

$$\mathbf{F} = \mathbf{F}_{\text{el}} \mathbf{F}_{\text{ch}} \quad (2)$$

into a chemical part  $\mathbf{F}_{\text{ch}}$ , caused by lithium uptake of the host material, and an elastic part  $\mathbf{F}_{\text{el}}$ , caused by mechanical stress. We assume an isotropic and linear chemical expansion of the host material with rising lithium content according to

$$\mathbf{F}_{\text{ch}} = \lambda_{\text{ch}} \mathbf{Id} \quad \text{with} \quad \lambda_{\text{ch}} = \sqrt[3]{1 + \nu c} \quad (3)$$

Here,  $\nu$  denotes the partial molar volume of lithium inside the host material and  $c$  the lithium concentration. In the following subsections, we derive the balance equations in the non-deforming reference configuration  $\Omega_0$ .

### 2.2. Phase-Field Model

#### 2.2.1. Free Energy Density

We derive a thermodynamically consistent model based on a free energy density  $\psi$ , which guarantees a strictly positive entropy production.<sup>[37]</sup> The free energy density consists of a chemical part  $\psi_{\text{ch}}$ , an interfacial part  $\psi_{\text{int}}$ , and an elastic part  $\psi_{\text{el}}$ .<sup>[11,17,24,26]</sup>

$$\psi = \psi_{\text{ch}} + \psi_{\text{int}} + \psi_{\text{el}} \quad (4)$$

The chemical free energy density  $\psi_{\text{ch}}$  has the form

$$\psi_{\text{ch}} = RTc_{\text{max}} \left[ \alpha_1 \bar{c} + \frac{\alpha_2}{2} \bar{c}^2 + \bar{c} \log(\bar{c}) + (1 - \bar{c}) \log(1 - \bar{c}) \right] \quad (5)$$

depending on the normalized lithium concentration  $\bar{c} = c/c_{\text{max}}$  with the maximum lithium concentration of the host material  $c_{\text{max}}$ , the universal gas constant  $R$ , and the operation temperature  $T$  in Kelvin. The first two terms account for the energetic contributions from the interaction of lithium ions with the host material ( $\alpha_1$ ) and other lithium ions ( $\alpha_2$ ).<sup>[24,31,38]</sup> Thereby, these parameters determine the equilibrium

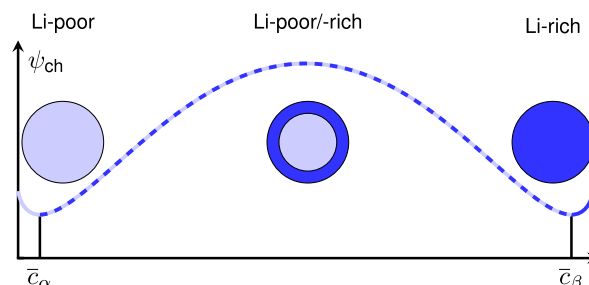


**Figure 2.** Upon lithium uptake, the particle separates into a lithium poor  $\alpha$ -phase and a lithium rich  $\beta$ -phase. The normalized lithium concentrations  $\bar{c}_\alpha$  and  $\bar{c}_\beta$  of the respective phase is set by the minima of the double well potential.

concentrations  $\bar{c}_\alpha$  and  $\bar{c}_\beta$ . The third and fourth term describe the entropic contributions based on a solid solution approach. These interactions lead to a double well potential, as shown in **Figure 2**, with two stable phases  $\alpha$  and  $\beta$ .<sup>[11,24,31]</sup>

The interfacial energy functional

$$\psi_{\text{int}} = \frac{1}{2} RT c_{\text{max}} \kappa |\nabla \bar{c}|^2 \quad (6)$$

gives rise to a separation of these phases. The interfacial energy coefficient  $\kappa$  determines the magnitude of the interfacial energy and thereby the interface thickness  $s$ <sup>[15]</sup> according to

$$s = (\bar{c}_\beta - \bar{c}_\alpha) \sqrt{\frac{\kappa}{2\Delta\bar{\psi}_{\text{ch}}}} \quad (7)$$

with the normalized equilibrium concentrations of the lithium poor  $\bar{c}_\alpha$  and lithium rich phase  $\bar{c}_\beta$ . The excess free energy density  $\Delta\bar{\psi}_{\text{ch}}$  is defined as the difference of the normalized chemical free energy density  $\bar{\psi} = \psi/RTc_{\text{max}}$  at  $(\bar{c}_\alpha + \bar{c}_\beta)/2$  and the normalized chemical free energy density obtained as mixture of the  $\alpha$  and  $\beta$  phases<sup>[32]</sup>

$$\Delta\bar{\psi}_{\text{ch}} = \bar{\psi}_{\text{ch}}\left(\frac{\bar{c}_\alpha + \bar{c}_\beta}{2}\right) - \frac{1}{2}(\bar{\psi}_{\text{ch}}(\bar{c}_\alpha) + \bar{\psi}_{\text{ch}}(\bar{c}_\beta)) \quad (8)$$

We describe the elastic energy inside the host material with a linear elastic approach<sup>[35,36]</sup>

$$\psi_{\text{el}} = \frac{1}{2} \mathbf{E}_{\text{el}} : \mathbf{C} \mathbf{E}_{\text{el}} \quad \text{with} \quad \mathbf{C} \mathbf{E}_{\text{el}} = \lambda \text{tr}(\mathbf{E}_{\text{el}}) \mathbf{Id} + 2G \mathbf{E}_{\text{el}} \quad (9)$$

where  $\lambda = 2G\nu/(1 - 2\nu)$  and  $G = E_{\text{H}}/(2(1 + \nu))$  are the Lamé constants, which depend on the elastic modulus  $E_{\text{H}}$  and Poisson's ratio  $\nu$  of the host material.

We define the elastic strain  $\mathbf{E}_{\text{el}}$  as the difference between total  $\mathbf{C}$  and stress-free chemical deformation  $\mathbf{C}_{\text{ch}}$  with the deformation gradients  $\mathbf{F}$  and  $\mathbf{F}_{\text{ch}}$  defined by Equation (1) and (3)

$$\mathbf{E}_{\text{el}} = \frac{1}{2} (\mathbf{C} - \mathbf{C}_{\text{ch}}) \quad \text{with} \quad \mathbf{C} = \mathbf{F}^T \mathbf{F} \quad \text{and} \quad \mathbf{C}_{\text{ch}} = \mathbf{F}_{\text{ch}}^T \mathbf{F}_{\text{ch}} \quad (10)$$

Based on this free energy density, we proceed to derive constitutive equations to describe the coupling of chemistry and mechanics.

### 2.2.2. Chemistry

The lithium concentration inside the host changes over time due to a gradient in the lithium flux  $\mathbf{N}$

$$\partial_t \bar{c} = -\nabla \cdot \mathbf{N} \quad (11)$$

At the particle boundary, we neglect surface wetting<sup>[39]</sup> and apply a uniform and constant external flux  $N_{\text{ext}}$ . We measure this flux in terms of the C-rate, which describes the hours it takes to fully charge the particle,  $t_{\text{cycle}} = 1/\text{C-rate}$ . The external flux in C is transformed to SI units by

$$|N_{\text{ext}}| [\text{mol m}^{-2} \text{s}^{-1}] = \frac{1 \text{ h}}{3600 \text{ s}} \frac{c_{\text{max}}}{A_{\text{V}}} N_{\text{ext}} [\text{C}] \quad (12)$$

with the specific surface  $A_{\text{V}} = S/V$  in  $\text{m}^2 \text{m}^{-3}$ . Using the C-rate, we obtain the *state of charge* (SOC) of the particle by

$$\text{SOC} = \frac{1}{V} \int_{\Omega_0} \bar{c} d\mathbf{X}_0 = \bar{c}_0 + N_{\text{ext}} [\text{C}] \cdot t [\text{h}] \quad (13)$$

with the normalized initial concentration  $\bar{c}_0$ .

Inside the particle, a gradient in the chemical potential  $\mu$  drives the lithium flux according to

$$\mathbf{N} = -m(\bar{c}) \nabla \mu \quad (14)$$

with the isotropic mobility  $m$  of the lithium atoms inside the host material. Following Di Leo et al.,<sup>[26]</sup> we define the mobility as

$$m(\bar{c}) = \frac{D c_{\text{max}}}{RT} \bar{c} (1 - \bar{c}) \quad (15)$$

with the diffusion coefficient  $D$  of lithium atoms inside the host material.

We determine the chemical potential as variational derivative of the system's free energy  $\Psi = \int_{\Omega_0} \psi d\mathbf{X}_0$  with respect to the lithium concentration  $c$ <sup>[40]</sup>

$$\begin{aligned} \mu &= \partial_c \psi - \nabla \cdot \partial_{\nabla c} \psi \\ &= RT \left[ \alpha_1 + \alpha_2 \bar{c} + \log\left(\frac{\bar{c}}{1 - \bar{c}}\right) \right] - \frac{\nu}{3\lambda_{\text{ch}}} \text{tr}(\mathbf{C} \mathbf{E}_{\text{el}}) - RT \kappa \Delta \bar{c} \end{aligned} \quad (16)$$

### 2.2.3. Mechanics

Mechanical stresses arise inside the host material due to large deformations during lithiation. We describe the mechanics with the momentum balance in the reference configuration  $\Omega_0$

$$\nabla \cdot \mathbf{P} = 0 \quad (17)$$

which neglects body and inertial forces. Here,  $\mathbf{P} = \det(\mathbf{F}) \boldsymbol{\sigma} \mathbf{F}^{-T}$  denotes the first Piola–Kirchhoff stress tensor, which is the transformation of the Cauchy stress  $\boldsymbol{\sigma}$  to the reference configuration. We determine the first Piola–Kirchhoff stress tensor  $\mathbf{P}$  thermodynamically consistent as the partial derivative of the free energy with respect to the deformation gradient  $\mathbf{F}$ <sup>[36]</sup>

$$\mathbf{P} = \partial_{\mathbf{F}} \psi = \mathbf{F} \mathbf{C} \mathbf{E}_{\text{el}} \quad (18)$$

## 3. Numerical Treatment

In this section we first introduce the normalization of the model equations from Section 2 and state the mathematical problem summarizing all equations in an initial boundary value problem. Afterward, we describe the space and time discretization with finite elements and a family of multistep methods. Finally, we present and explain the space and time adaptive solution algorithm, which we will use for our numerical experiments in Section 4.

### 3.1. Mathematical Problem Formulation

#### 3.1.1. Normalization

We normalize the underlying model equations to improve the numerical simulation stability. We define the length scale of the reference configuration  $L_0$  as reference for the spatial scale, the cycle time  $t_{\text{cycle}}$  for the time scale, and the maximum lithium concentration  $c_{\text{max}}$  as reference concentration. We normalize the energy density using  $RTc_{\text{max}}$ . **Table 1** shows the arising dimensionless quantities.

The normalization yields three dimensionless parameters characterizing the chemical–mechanical intercalation process: The *Fourier number* of mass transport  $\text{Fo}$  relates the diffusion time scale to the process time scale. The numbers  $\tilde{E}_{\text{H}}$  and  $\tilde{\kappa}$  relate the mechanical and the interfacial energy scale to the chemical energy scale.

In the following, we consider the model equations in terms of these dimensionless quantities and suppress the accentuation  $\sim$  to enhance readability.

#### 3.1.2. Problem Statement

For the mathematical problem formulation, we introduce the chemical potential  $\mu$  as additional solution variable to circumvent the regularity requirements on the finite element method imposed by the higher order differential operators. Thus, we split the fourth-order diffusion equation into two second-order equations.<sup>[17,30]</sup>

To simplify the model equations further, we express the stress and strain tensors  $\mathbf{P}$ ,  $\mathbf{E}_{\text{el}}$  as well as the deformation gradient  $\mathbf{F}$  in terms of the displacement  $\mathbf{u}$ . We thus rely on the normalized concentration  $c$ , the chemical potential  $\mu$ , and the displacement  $\mathbf{u}$  as variables and recover the stress in a postprocessing step.

The resulting dimensionless initial boundary value problem then reads as: Let  $t_f > 0$  be the final simulation time and  $\Omega_0 \subset \mathbb{R}^3$  be the bounded domain representing the reference configuration of an arbitrarily shaped electrode particle. Find the normalized lithium concentration  $c: [0, t_f] \times \bar{\Omega}_0 \rightarrow [0, 1]$ , the chemical potential  $\mu: [0, t_f] \times \bar{\Omega}_0 \rightarrow \mathbb{R}$ , and the displacement  $\mathbf{u}: [0, t_f] \times \bar{\Omega}_0 \rightarrow \mathbb{R}^3$ , up to rigid body motions, satisfying

$$\begin{cases} \partial_t c = -\nabla \cdot \mathbf{N}(c, \mu) & \text{in } (0, t_f) \times \Omega_0 \\ \mu = \partial_c \psi(c, \nabla c, \nabla \mathbf{u}) \\ \quad - \nabla \cdot \partial_{\nabla c} \psi(c, \nabla c, \nabla \mathbf{u}) & \text{in } (0, t_f) \times \Omega_0 \\ \nabla \cdot \mathbf{P}(c, \nabla \mathbf{u}) = 0 & \text{in } (0, t_f) \times \Omega_0 \\ \nabla c \cdot \mathbf{n} = 0 & \text{on } (0, t_f) \times \partial \Omega_0 \\ \mathbf{N}(c, \mu) \cdot \mathbf{n} = N_{\text{ext}} & \text{on } (0, t_f) \times \partial \Omega_0 \\ \mathbf{P}(c, \nabla \mathbf{u}) \cdot \mathbf{n} = 0 & \text{on } (0, t_f) \times \partial \Omega_0 \\ c(0, \cdot) = c_0 & \text{in } \Omega_0 \end{cases} \quad (19)$$

**Table 1.** Normalization of basic model parameters.

$\tilde{t} = t/t_{\text{cycle}}$	$\tilde{\mathbf{x}}_0 = \mathbf{x}_0/L_0$	$\tilde{\mathbf{u}} = \mathbf{u}/L_0$	$\tilde{c} = c/c_{\text{max}}$	$\tilde{\mu} = \mu/RT$
$\tilde{\nu} = \nu c_{\text{max}}$	$\tilde{\psi} = \psi/RTc_{\text{max}}$	$\tilde{N}_{\text{ext}} = N_{\text{ext}}t_{\text{cycle}}/L_0c_{\text{max}}$		
$\text{Fo} = Dt_{\text{cycle}}/L_0^2$	$\tilde{\kappa} = \kappa/L_0^2$	$\tilde{E}_{\text{H}} = E_{\text{H}}/RTc_{\text{max}}$		

where we assume the initial condition  $c_0$  to be consistent with the boundary conditions.

### 3.2. Numerical Solution Method

In a straightforward way, we extend our discretization scheme from the study by Castelli and Dörfler.<sup>[41]</sup>

#### 3.2.1. Space and Time Discretization

To derive the spatial discrete formulation, we first multiply the partial differential equations of (19) with test functions and integrate over the reference domain  $\Omega_0$ . Integration by parts yields the weak formulation with the solutions  $c, \mu \in V$ , and  $\mathbf{u} \in V^*$  with suitable function spaces.<sup>[35]</sup> The space  $V^*$  incorporates appropriate displacement constraints, which will be specified later for the precise application case in Subsection 4.1. To abbreviate our notation, we denote  $(f, g) = \int_{\Omega_0} fgd\mathbf{X}_0$  as the  $L^2$ -inner product for two functions  $f, g \in L^2(\Omega_0)$  as well as  $(\mathbf{v}, \mathbf{w}) = \int_{\Omega_0} \mathbf{v} \cdot \mathbf{w}d\mathbf{X}_0$  for two vectors  $\mathbf{v}, \mathbf{w} \in L^2(\Omega_0; \mathbb{R}^3)$  and  $(\mathbf{S}, \mathbf{T}) = \int_{\Omega_0} \mathbf{S} : \mathbf{T}d\mathbf{X}_0$  for two tensors  $\mathbf{S}, \mathbf{T} \in L^2(\Omega_0; \mathbb{R}^{3,3})$ . We indicate boundary integrals with the subscript  $\partial \Omega_0$ .

For the application of the isoparametric Lagrangian finite element method<sup>[35]</sup> we replace the domain  $\Omega_0$  of the reference configuration by a computational domain  $\Omega_h$ , which we assume to be a polytop with appropriate boundary approximation of curved boundaries. Next, we chose an admissible mesh  $\mathcal{T}_h$  of the computational domain  $\Omega_h$  and assume  $V_h \subset V$  and  $V_h^* \subset V^*$  to be finite dimensional subspaces with bases  $\{\varphi_i \in V_h: i = 1, \dots, N_x\}$  and  $\{\xi_i \in V_h^*: i = 1, \dots, 3N_x\}$ . Now, we seek  $c_h: [0, t_f] \rightarrow \{c_h \in V_h: c_h(x) \in [0, 1]\}$ ,  $\mu_h: [0, t_f] \rightarrow V_h$ ,  $\mathbf{u}_h: [0, t_f] \rightarrow V_h^*$  to be solutions of the spatial discrete problem

$$\begin{cases} (\varphi_i, \partial_t c_h) = -(\nabla \varphi_i, m(c_h)\nabla \mu_h) - (\varphi_i, N_{\text{ext}})_{\partial \Omega_0} \\ 0 = -(\varphi_j, \mu_h) + (\varphi_j, \partial_c \psi_{\text{ch}}(c_h) + \partial_c \psi_{\text{el}}(c_h, \nabla \mathbf{u}_h)) + \kappa(\nabla \varphi_j, \nabla c_h) \\ 0 = -(\nabla \xi_k, \mathbf{P}(c_h, \nabla \mathbf{u}_h)) \end{cases} \quad (20)$$

for all  $i, j = 1, \dots, N_x$  and  $k = 1, \dots, 3N_x$ . We insert the finite element ansatz, namely, the basis representation of the solution variables

$$c_h(t, \mathbf{x}) = \sum_{i=1}^{N_x} c_i(t)\varphi_i(\mathbf{x}) \quad (21)$$

$$\mu_h(t, \mathbf{x}) = \sum_{i=1}^{N_x} \mu_i(t)\varphi_i(\mathbf{x}), \quad (22)$$

$$\mathbf{u}_h(t, \mathbf{x}) = \sum_{i=1}^{3N_x} \mathbf{u}_i(t)\xi_i(\mathbf{x}) \quad (23)$$

and gather the time-dependent coefficients in a common vector-valued function

$$\mathbf{y}: [0, t_f] \rightarrow \mathbb{R}^{(2+3)N_x} \quad t \mapsto \mathbf{y}(t) = [(c_i(t))_i, (\mu_i(t))_i, (\mathbf{u}_i(t))_i]^T \quad (24)$$

such that we can reformulate the spatially discrete problem (20) as general nonlinear differential algebraic equation (DAE): Find

$\mathbf{y}: [0, t_f] \rightarrow \mathbb{R}^{5N_x}$  satisfying

$$\mathbf{M} \partial_t \mathbf{y} = \mathbf{f}(t, \mathbf{y}) \quad \text{for } t \in (0, t_f] \quad \mathbf{y}(0) = \mathbf{y}^0 \quad (25)$$

The mass matrix of the DAE is singular with its only nonzero block entry  $\mathbf{M}_{11} = [(\varphi_i, \varphi_j)]_{ij}$  denoting the mass matrix of the finite element space  $V_h$ . The right hand side is defined according to the weak formulation (20): with  $\mathbf{y}$  related to  $c_h, \mu_h, \mathbf{u}_h$  as described, we have  $\mathbf{f}: [0, t_f] \times \mathbb{R}^{5N_x} \rightarrow \mathbb{R}^{5N_x}$

$$\mathbf{f}(t, \mathbf{y}) := \begin{pmatrix} -K_m(c_h)\mu_h - N_{\text{ext}} \\ -M\mu_h + \Psi_{\text{ch}}(c_h) + \Psi_{\text{el}}(c_h, \nabla \mathbf{u}_h) + \kappa K_1 c_h \\ -\Sigma(c_h, \nabla \mathbf{u}_h) \end{pmatrix} \quad (26)$$

with the matrices

$$M = [(\varphi_i, \varphi_j)]_{ij} \quad (27)$$

$$K_1 = [(\nabla \varphi_i, \nabla \varphi_j)]_{ij} \quad (28)$$

$$K_m(c_h) = [(\nabla \varphi_i, m(c_h) \nabla \varphi_j)]_{ij} \quad (29)$$

and the vectors for the nonlinearities and the boundary condition

$$\Psi_{\text{ch}}(c_h) = [(\varphi_j, \partial_c \psi_{\text{ch}}(c_h))]_j \quad (30)$$

$$\Psi_{\text{el}}(c_h, \nabla \mathbf{u}_h) = [(\varphi_j, \partial_c \psi_{\text{el}}(c_h, \nabla \mathbf{u}_h))]_j \quad (31)$$

$$\Sigma(c_h, \nabla \mathbf{u}_h) = [(\nabla \xi_k, \mathbf{P}(c_h, \nabla \mathbf{u}_h))]_k \quad (32)$$

$$N_{\text{ext}} = [(\varphi_i, N_{\text{ext}})_{\partial \Omega_0}]_i \quad (33)$$

with the ranges of the indices  $i, j, k$  as above.

The resulting DAE (25) can be treated similar to a stiff ordinary differential equation. Therefore, we employ the family of numerical differentiation formulas in a variable-step, variable-order algorithm, in Matlab known as ode15s.<sup>[42–45]</sup> Thereby, the time step size and the order are adaptively changed by an error control.

Finally, the space and time discrete problem for advancing one time step from time  $t_n$  to  $t_{n+1} = t_n + \tau_n$  with the time step size  $\tau_n > 0$  is to find the discrete solution  $\mathbf{y}^{n+1} \approx \mathbf{y}(t_{n+1})$  satisfying

$$\xi_k \mathbf{M}(\Phi^n + \mathbf{y}^{n+1}) = \tau_n \mathbf{f}(t_{n+1}, \mathbf{y}^{n+1}) \quad (34)$$

with  $\Phi^n$  depending on the solutions at some previous time steps  $\mathbf{y}^n, \dots, \mathbf{y}^{n-k}$  and a constant  $\xi_k > 0$  for the chosen order  $k$  [Ref. 43, Sect. 2.3].

### 3.2.2. Space and Time Adaptive Algorithm

We use a revised version of the space and time adaptive solution algorithm already used in the study by Castelli and Dörfler<sup>[41]</sup> for the simulation of phase separation in electrode particles without mechanical coupling, see Algorithm 1. In the following we discuss some single steps and refer to Ref. [46] for further details.

In Line 2 we linearize the nonlinear algebraic system (34) using the Newton–Raphson method and solve for the updates with a direct LU-decomposition. Note that a suitable initialization

**Algorithm 1.** Space and time adaptive solution algorithm.

---

```

1: Given  $\mathcal{T}_n, \tau_n, k$  and  $\mathbf{y}^n, \dots, \mathbf{y}^{n-k}$ 
2: Solve for  $\mathbf{y}^{n+1}$ 
3: Estimate time error  $\text{err}_t$  and spatial regularity  $\text{est}_x$ 
4: if  $\text{err}_t < \text{RelTol}_t$  and  $\text{est}_x < \text{RelTol}_x$ , then
5:   Continue with Line 15
6: else
7:   if  $\text{err}_t > \text{RelTol}_t$ , then
8:     Adapt time step size  $\tau_{n+1}$  and order  $k$ 
9:   end if
10:  if  $\text{est}_x > \text{RelTol}_x$ , then
11:    Mark elements and refine mesh  $\mathcal{T}_{n+1}$ 
12:  end if
13:  Go to Line 2
14: end if
15: Update solution  $\mathbf{y}^{n+1} \rightarrow \mathbf{y}^n$  and time  $t_{n+1} = t_n + \tau_n \rightarrow t_n$ 
16: if a sufficient number of time steps were accepted try coarsening, then
17:   Adapt time step size  $\tau_{n+1}$  and order  $k$ 
18:   Mark elements and coarsen mesh  $\mathcal{T}_{n+1}$ 
19: end if
20: Advance time step

```

---

of the Newton–Raphson method reduces the number of iteration steps. During the time integration we use the predictor of the scheme<sup>[43]</sup> for the initialization. The starting values of the Newton–Raphson method used for the first time step are given later in Subsection 4.1.

The estimation of the temporal error in Line 3 is incorporated in the time integration method.<sup>[42–45]</sup> We measure the spatial regularity using a gradient recovery estimator [Ref. 47, Chap. 4]. For a general finite element solution  $v_h$  (here  $c_h, \mu_h$ , or  $\mathbf{u}_h$ ), we recover the gradient  $G(v_h)$  in the finite element space of  $v_h$ , as in the study by Castelli and Dörfler.<sup>[41]</sup> Therefore, we define local estimates for each element  $Q$  of the mesh  $\mathcal{T}_n$  by

$$\eta_Q^2(v_h) := \int_Q |G(v_h) - \nabla v_h|^2 dx \quad (35)$$

and the global estimate

$$\text{est}_x := \left( \sum_{Q \in \mathcal{T}_n} \eta_Q^2 \right)^{1/2} \quad (36)$$

with

$$\eta_Q^2 := \eta_Q^2(c_h) + \eta_Q^2(\mu_h) + \eta_Q^2(\mathbf{u}_h) \quad (37)$$

In Line 8 and 17 we change the time step size and order adaptively according to Refs. [42–45]. For the spatial marking in Line 11 and 18, we use a maximum strategy according to Bañas and Nürnberg.<sup>[48]</sup> Thereby, we introduce the two parameters  $\theta_c$  and  $\theta_r$  controlling the amount of cells that are locally coarsened or refined.

Note that the temporal error and the spatial regularity estimates of Line 3 are multiplied by weights  $\omega_t, \omega_x$  such that we realize a mixed error control, compare [Ref. 45, Chap. 1.4], with  $\text{RelTol}_t, \text{AbsTol}_t$  and  $\text{RelTol}_x, \text{AbsTol}_x$ .

## 4. Numerical Experiments

In the following section we present and discuss the results of our numerical experiments obtained with the adaptive finite element solver from Section 3 for the model developed in Section 2. Therefore we first specify the simulation setup in Subsection 4.1. The discussion of the results is then split into a physical analysis in Subsection 4.2 and a numerical analysis of the efficiency in Subsection 4.3.

### 4.1. Simulation Setup

Throughout the numerical experiments we apply the so far generally derived formalism to the lithiation of a LFP electrode particle<sup>[23–30]</sup> with the model parameters and their normalized value given in **Table 2**, corresponding to the external lithium flux  $N_{\text{ext}} = 1\text{C}$ .

As an exemplary particle geometry, we consider a spherical electrode particle and assume a radial symmetric solution. Thus, the 3D geometry reduces to the radial direction. A final 2D example will demonstrate the capabilities and superior efficiency of our numerical solution method.

In the following we define the additional boundary conditions for both geometries based on symmetry arguments and briefly discuss some further implementation details.

#### 4.1.1. Radial Symmetry

The computational domain becomes the 1D unit interval  $\Omega_0 = (0, 1)$ , representing a radial line from the particle center

**Table 2.** Model parameters for a LFP particle.

Description	Symbol	Value	Unit	Dimensionless	Source
Operation temperature	$T$	298.15	K	1	Chosen
Particle length scale	$L_0$	$150 \times 10^{-9}$	m	1	Chosen
Diffusion coefficient	$D$	$1 \times 10^{-15}$	$\text{m}^2 \text{s}^{-1}$	$1.6 \times 10^2$	[49]
Coefficient for $\psi_{\text{ch}}$	$\alpha_1$	4.5	–	4.5	[27]
Coefficient for $\psi_{\text{ch}}$	$\alpha_2$	-9	–	-9	[27]
Interfacial energy coefficient	$\kappa$	$8.8 \times 10^{-18}$	$\text{m}^2$	$3.91 \times 10^{-4}$	[27]
Young's modulus	$E_{\text{H}}$	$124.5 \times 10^9$	Pa	$2.19 \times 10^3$	[50]
Poisson ratio	$\nu$	0.26	–	0.26	[50]
Partial molar volume	$\nu$	$2.9 \times 10^{-6}$	$\text{m}^3 \text{mol}^{-1}$	$6.64 \times 10^{-2}$	[51]
Maximal concentration	$c_{\text{max}}$	$2.29 \times 10^4$	$\text{mol m}^{-3}$	1	[51]
Initial concentration	$c_0$	$2.29 \times 10^2$	$\text{mol m}^{-3}$	$1 \times 10^{-2}$	Chosen

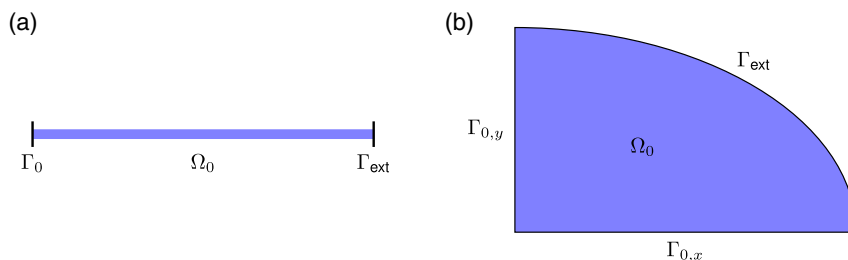


**Figure 3.** a) 1D radial particle domain and b) 2D quarter domain of the cross section of a spheroidal particle.

$\Gamma_0 = \{0\}$  to the surface  $\Gamma_{\text{ext}} = \{1\}$  (see **Figure 3a**). At the artificial boundary in the particle center, we assume a natural boundary condition for the concentration, a no-flux condition for the lithium flux, and fix the radial displacement

$$\nabla c \cdot \mathbf{n} = 0 \quad \mathbf{N} \cdot \mathbf{n} = 0 \quad \mathbf{u} = \mathbf{0} \quad \text{on } (0, t_f) \times \Gamma_0 \quad (38)$$

We translate the radial symmetry into the discrete finite element formulation by using the modified quadrature weight  $d\mathbf{X}_0 = 4\pi r^2 dr$ . Assuming radial symmetry and a constant initial concentration  $c_0$ , an appropriate starting value for the Newton–Raphson method at the first time step is given by  $c_0$ , the constant chemical potential  $\mu_0 = \partial_c \psi_{\text{ch}}(c_0)$ , and the stress-free radial displacement  $\mathbf{u}_0(r) = r(\lambda_{\text{ch}}(c_0) - 1)$ .

#### 4.1.2. Spheroidal Electrode Particle

We consider the quarter of the cross section of a spheroidal particle (quarter of an ellipse) with a fraction of the semi-axes 1:0.6 (see **Figure 3b**), inspired by Di Leo et al.<sup>[26]</sup> We generate two flat boundaries  $\Gamma_{0,x}$  and  $\Gamma_{0,y}$  at the semi-axes and one curved boundary  $\Gamma_{\text{ext}}$  representing the particle surface, which we approximate with an isoparametric mapping. On the semi-axes we assume natural boundary conditions for the concentration and a vanishing lithium flux. The displacement on the semi-axes is only allowed in the radial direction. Summing up we have the following artificial boundary conditions

$$\begin{aligned} \nabla c \cdot \mathbf{n} = 0 & \quad \text{on } (0, t_f) \times \Gamma_0, & \mathbf{u}_y = 0 & \quad \text{on } (0, t_f) \times \Gamma_{0,x} \\ \mathbf{N} \cdot \mathbf{n} = 0 & \quad \text{on } (0, t_f) \times \Gamma_0, & \mathbf{u}_x = 0 & \quad \text{on } (0, t_f) \times \Gamma_{0,y} \end{aligned} \quad (39)$$

For this geometry we initialize the Newton–Raphson method at the first time step with the given constant initial concentration  $c_0$  along with  $\mu_0 = 0$  and  $\mathbf{u}_0 = \mathbf{0}$ .

#### 4.1.3. Mesh Width

For the accurate resolution of the phase transition, we distribute at least ten degrees of freedom (DOFs) inside the interfacial zone. Following Equation (7), we determine the dimensionless interface thickness  $s \approx 0.02$ . Thus, we obtain the estimate  $h < 0.02p/10$  for the minimal mesh width, knowing that for a  $p$ -th order Lagrangian finite element method the approximate distance of two DOFs is about  $h/p$ .

#### 4.1.4. Solver Parameters

We employ fourth-order isoparametric Lagrangian finite elements for all numerical experiments. In addition, we use for the adaptive space–time algorithm the tolerances  $\text{RelTol}_t = \text{RelTol}_x = 10^{-5}$ ,  $\text{AbsTol}_t = \text{AbsTol}_x = 10^{-8}$  and the marking parameters for local coarsening  $\theta_c = 0.05$  and refinement  $\theta_r = 0.5$ . Solely for the simulation to Figure 5 we deviate and use a uniform mesh ( $h = 2^{-7}$ ) because the strongly varying C-rates would require different tolerances for spatial adaptivity.

#### 4.1.5. Implementation

We implement the numerical methods described in Section 3 as C++ code based on the functionalities of the finite element library *deal.II*<sup>[52]</sup> and the direct LU-decomposition of the UMFPACK package.<sup>[53]</sup> We execute the simulations on a laptop pc with 4 GB RAM and four Intel i5-4200U CPUs with 1.6 GHz. For the 2D simulation, we instead use a node of a cluster with 96 GB RAM and 20 Intel Xeon Silver 4114 CPUs with 2.2 GHz. To speed up the computational time, we enable shared memory parallelization for the assembly of the system matrices, residuals, and spatial estimates.

## 4.2. Chemomechanics

In this subsection, we analyze the relationship between phase separation and mechanical stress. We start by investigating the stress evolution during lithiation. Afterward, we look at the development of the maximum stress inside the particle for different charging rates. We then analyze the influence of the interface properties on the mechanical stress and conclude

with the investigation of the chemical potential during charging and discharging.

#### 4.2.1. Lithium Insertion

In **Figure 4**, we see the normalized concentration  $c$  and the radial  $\sigma_r$ , tangential  $\sigma_\phi$  as well as hydrostatic stress  $\sigma_h = 1/3\sigma_r + 2/3\sigma_\phi$  inside the particle during lithium insertion with  $N_{\text{ext}} = 1 \text{ C}$ . We observe three different states throughout lithiation. First, for  $\text{SOC} \lesssim 0.2$ , the particle exhibits only a single phase and the stress magnitude is low. Second, for  $0.2 \lesssim \text{SOC} \lesssim 0.94$ , the particle separates into a lithium poor phase and a lithium rich phase. Figure 4a shows the emergence of both phases, which develop to the concentration distribution shown in Figure 4b. Along the phase boundary, a sharp transition of the concentration and the hydrostatic stress from tensile (lithium poor phase) to compressive (lithium rich phase) occurs. Third, if  $\text{SOC} \gtrsim 0.94$ , the lithiation of the lithium poor phase sets in and the phase boundary vanishes, as shown in Figure 4c. The stress in the lithium poor part remains tensile, whereas the stress in the lithium rich part vanishes.

We observe a tensile stress in the lithium poor phase and a compressive stress in the lithium rich phase because the different degrees of lithiation cause a volume mismatch inside the particle. The elastic deformation compensates this trend by compressing the lithium rich phase and expanding the lithium poor phase. This leads to a sharp drop of the tangential stress  $\sigma_\phi$  from tensile to compressive at the interface. The radial stress  $\sigma_r$ , in contrast, shows a continuous transition across the interface to fulfill the mechanical equilibrium.

Comparing our results for the mechanical stress with the literature, we see that the radial and the tangential stresses are in excellent qualitative agreement with Walk et al.<sup>[11]</sup> Likewise, the

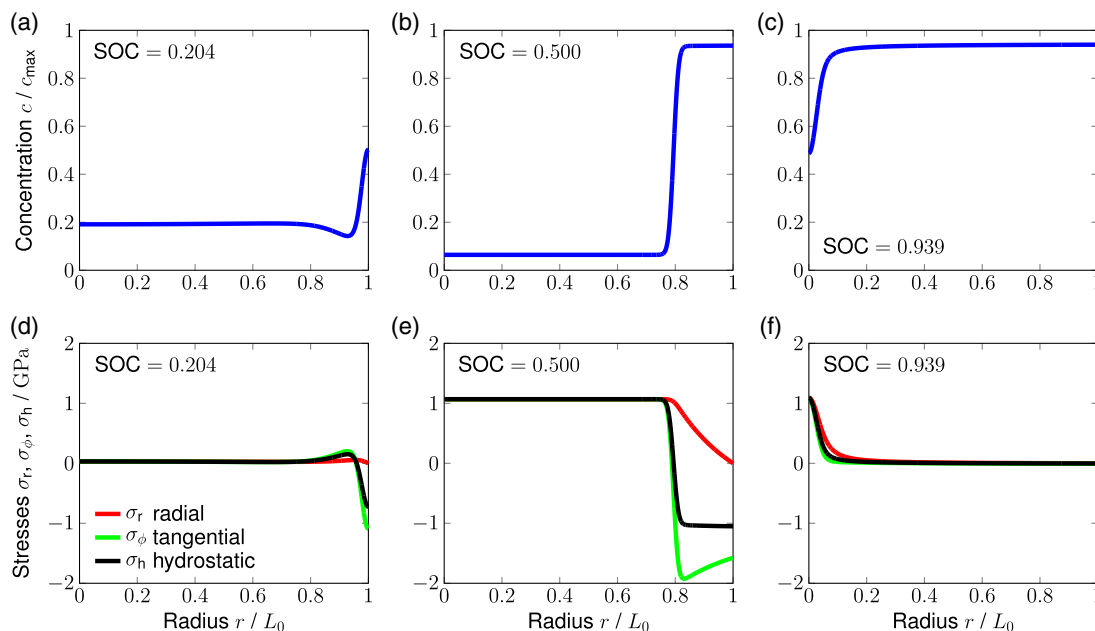


**Figure 4.** Concentration (top) and radial  $\sigma_r$ , tangential  $\sigma_\phi$ , and hydrostatic stresses  $\sigma_h$  (bottom) inside the particle at three characterizing SOC for lithium insertion. a,d) Initiation of phase separation. b,e) Migration of the phase transition. c,f) Vanishing of the phase transition.

hydrostatic stress shows the same qualitative behavior as in Zhang and Kamlah.<sup>[23–25]</sup>

#### 4.2.2. Maximum Stress

*Variation of the C-rate:* In **Figure 5**, we present the maximum stress for different SOC and charging rates. **Figure 5a** shows the absolute value of the maximum hydrostatic stress  $|\sigma_{h,max}|$  inside the particle during charging with various C-rates. Again, we identify the three distinct states ( $SOC \lesssim 0.2$ ,  $0.2 \lesssim SOC \lesssim 0.94$ ,  $0.94 \lesssim SOC$ ). For low C-rates, the stress vanishes in the first and third state, which correspond to a purely lithium poor and rich phase. In the second state, however, a large hydrostatic stress emerges with two maxima at the phase separation ( $SOC \approx 0.2$ ), respective at the complete lithiation of the lithium poor phase ( $SOC \approx 0.94$ ), and a minimum in between. For higher C-rates, the end point of the simulation is shifted towards lower SOC. Moreover, the first phase ( $SOC \lesssim 0.2$ ) is less homogeneous and exhibits high stresses. In **Figure 5b**, we plot the maximum stress over the applied C-rate. We see that the stress approaches a constant value of  $|\sigma_{h,total}| \approx 2.15$  GPa for  $N_{ext} = 0$ , i.e., quasi-static charging. This stress is largely constant for low C-rates, but increases to a maximum of  $|\sigma_{h,total}| \approx 2.3$  GPa at  $N_{ext} = 10$  C. For higher C-rates, we first see a decrease to  $|\sigma_{h,total}| \approx 1.8$  GPa at about  $N_{ext} = 50$  C, followed by a continuous increase with rising  $N_{ext}$ .

As already discussed in **Figure 4**, inhomogeneous lithiation causes volume mismatches and thereby mechanical stress. For single phases, the concentration is distributed evenly for C-rates up to 10 C because  $Fo \gg 1$ . When the C-rate increases further, the lithium concentration becomes less homogeneous and thus gives rise to a hydrostatic stress, which increases with the C-rate. Upon the initial phase separation ( $SOC \approx 0.2$ ), a large compressive stress arises in the outer lithium rich phase. This stress decreases with increasing SOC because the size of the lithium rich phase approaches that of the lithium poor phase. Thereby, each element of the lithium poor phase is stretched further, while each element of the lithium rich phase is compressed less. At  $SOC \approx 0.5$ , compressive and tensile stress are equally large, leading to the observed minimum in **Figure 5a**. For higher SOC, the tensile stress in the particle center is the maximum absolute stress. This stress further increases with decreasing size

of the lithium poor phase, until the phase ultimately vanishes at  $SOC \approx 0.94$ .

The charging rate affects the maximum stress only weakly below  $N_{ext} = 0.1$  C (**Figure 5b**) because the phases are homogeneously lithiated due to  $Fo \gg 1$ . The sharp decrease in maximum stress for  $10\text{ C} < N_{ext} < 50\text{ C}$  comes from the premature end of the simulation. Thereby, the stress no longer reaches its maximum at  $SOC \approx 0.94$  and thus decreases until the compressive stress at the phase separation,  $SOC \approx 0.2$ , is the maximum stress. Higher charging currents  $N_{ext} > 50\text{ C}$  cause larger concentration gradients in the evolving lithium rich bulk phase. The simulation ends prematurely as the concentration reaches its maximum at the particle surface, so that the maximum arising stress occurs at the initiation of the phase separation.

Our results for the maximum absolute stress over SOC are in good qualitative accordance with the results of Zhang and Kamlah.<sup>[24]</sup> Likewise, the dependence of the maximum absolute stress on the charging rate accords to the work of Kamlah and co-workers.<sup>[11,21]</sup> However, we see that our solver exits prematurely above 10 C, as soon as the concentration reaches its maximum at the particle surface. We could resolve this issue by using Butler–Volmer boundary conditions instead of a constant charging rate.<sup>[26,39]</sup>

*Variation of the Interfacial Energy Coefficient:* Next, we analyze how the interfacial energy parameter  $\kappa$  influences the hydrostatic stress at the phase boundary. In **Figure 6a**, we see the dependence of the concentration profile on the interfacial energy quantified by the parameter  $\kappa$  for an SOC of 0.5. We observe that the phase separation becomes more diffuse with increasing  $\kappa$  up to a completely homogeneous concentration at  $\kappa/L_0^2 = 2 \times 10^{-1}$ . In **Figure 6b**, we plot the maximum resulting stress as a function of  $\kappa$ . We see that the arising stress is constant for several orders of magnitude,  $1 \times 10^{-5} < \kappa/L_0^2 < 5 \times 10^{-2}$ . For larger  $\kappa$ , the maximum stress sharply drops until it reaches approximately zero for  $\kappa/L_0^2 = 0.115$ .

The interface thickness depends on the interfacial energy coefficient according to  $s \sim \sqrt{\kappa}$  (see Equation (7)). The total stress  $|\sigma_{h,total}|$  decreases with increasing interface thickness  $s$  because the volume mismatches at more diffuse interfaces are weaker. For  $\kappa/L_0^2 = 0.115$ , the phase separation is completely suppressed because the energy penalty  $\sim \kappa|\nabla c|^2$  is higher than the energy gain of the separation into two phases. In this regime, the free

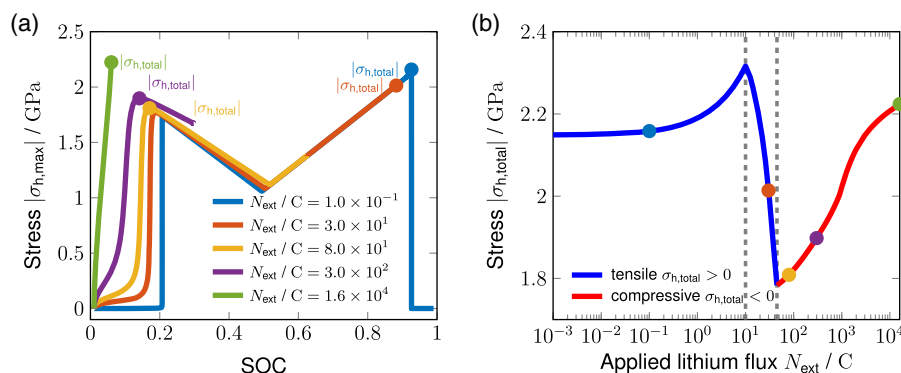


**Figure 5.** a) Maximal hydrostatic stress over SOC for different lithium insertion rates and b) maximal hydrostatic stress in the whole particle over applied C-rate coded with the same colors in both figures.



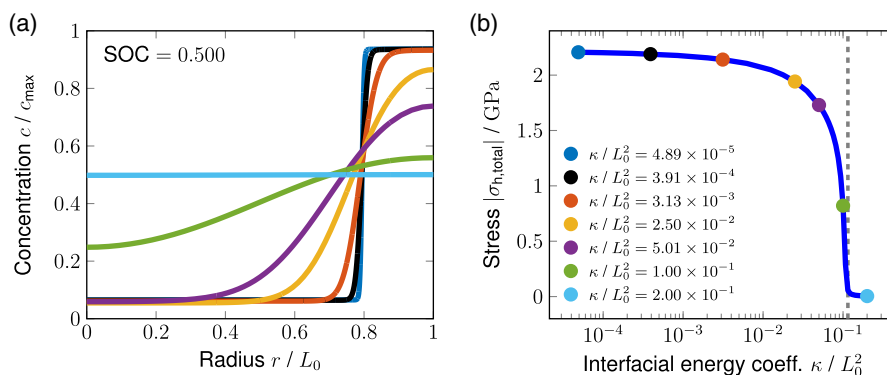


**Figure 6.** a) Phase transition and b) maximal arising hydrostatic stresses for varying phase-field parameter  $\kappa$  coded with the same colors in both figures.

**Table 3.** Normalized interfacethickness  $s/L_0$  in different simulations, calculated by Equation (7) with the respective parameters.

Material	Source	Coeff. $k$ [ $\text{m}^{-2}$ ]	Particle scale $L_0$ [ $\text{m}^{-1}$ ]	Interface thickness $s/L_0$
LMO	[11]	$7.0 \times 10^{-18}$	$1 \times 10^{-6}$	$6.4 \times 10^{-3}$
LMO	[32]	$4.2 \times 10^{-14}$	$1 \times 10^{-6}$	$5.4 \times 10^{-1}$
LFP	[24]	$8.8 \times 10^{-18}$	$150 \times 10^{-9}$	$2.0 \times 10^{-2}$
LFP	[39]	$8.8 \times 10^{-18}$	$100 \times 10^{-9}$	$3.1 \times 10^{-2}$
LFP	[26]	$2.5 \times 10^{-16}$	$500 \times 10^{-9}$	$5.7 \times 10^{-2}$
LFP	[30]	$2.7 \times 10^{-17}$	$40 \times 10^{-9}$	$1.0 \times 10^{-1}$
LFP	[54]	$4.1 \times 10^{-14}$	$1 \times 10^{-6}$	$2.8 \times 10^{-1}$

energy follows the profile shown in Figure 2 without undergoing the spinodal decomposition.<sup>[21,22]</sup>

Our concentration profiles are in good accordance with the results of Kamlah and co-workers<sup>[21,22]</sup> and show that the interface parameter  $\kappa$  is critical to determine the stress inside the particle. However, the values for  $\kappa$  vary throughout the literature as shown in Table 3.

3D particle simulations rely on a low computational expense of the problem. Thus, larger values for  $\kappa$  are used to increase the interface thickness and thereby the element size of the underlying mesh.<sup>[26,30,32,33]</sup> Based on Figure 6b, we argue that this approach underestimates the resulting stress at the interface.

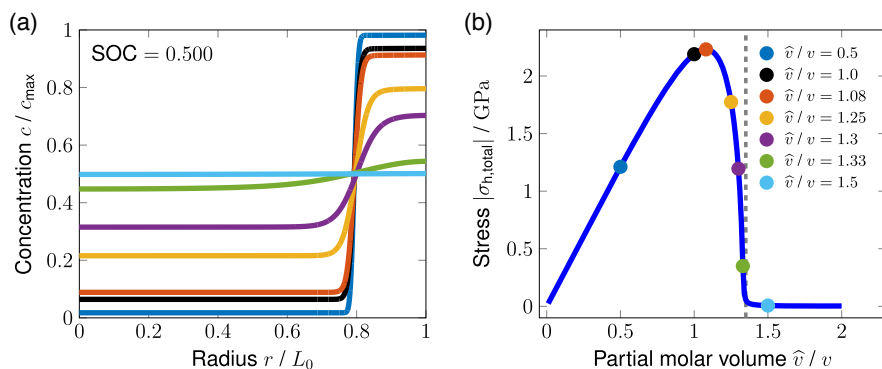


**Figure 7.** a) Phase transition and b) maximal arising hydrostatic stresses for varying partial molar volume  $\nu$  coded with the same colors in both figures.

**Variation of the Partial Molar Volume:** In Figure 7, we illustrate a sensitivity analysis of the partial molar volume  $\nu$ . Figure 7a shows the concentration profile along the particle for SOC = 0.5 for different values of  $\nu$ . We see that the interface becomes sharper for lower  $\nu$  and more diffuse for higher  $\nu$  until the profile degenerates to a single phase for  $\hat{\nu}/\nu = 1.5$ . In addition, the difference between the equilibrium concentrations shrinks with increasing  $\nu$ . Figure 7b shows the impact of  $\nu$  on the maximum hydrostatic stress during charging. We observe that the stress increases linearly with the partial molar volume up to its maximum at  $\hat{\nu}/\nu = 1.08$ . For larger  $\hat{\nu}$ , the stress sharply decays toward zero at  $\hat{\nu}/\nu \approx 1.35$ . Smaller partial molar volumes decrease the elastic deformation and thereby also the stress and the elastic free energy. Thus, more chemical excess free energy  $\Delta\bar{\psi}_{\text{ch}}$  converts into interfacial energy instead of elastic energy and the interface thickness becomes smaller. By increasing the partial molar volume, we revert this effect until the elastic free energy induced by phase separation is larger than  $\Delta\bar{\psi}_{\text{ch}}$ , so that phase separation is suppressed. This analysis shows that  $\nu$  is a key parameter of the model and requires precise determination.

#### 4.2.3. Hysteresis

Now, we investigate how mechanics influences the phase separation. In Figure 8, we illustrate the chemical part of the chemical potential,  $\mu_{\text{ch}} = \alpha_1 + \alpha_2\bar{c} + \log(\bar{c}/(1 - \bar{c}))$  in black and the simulated chemical potential during lithiation and delithiation in red

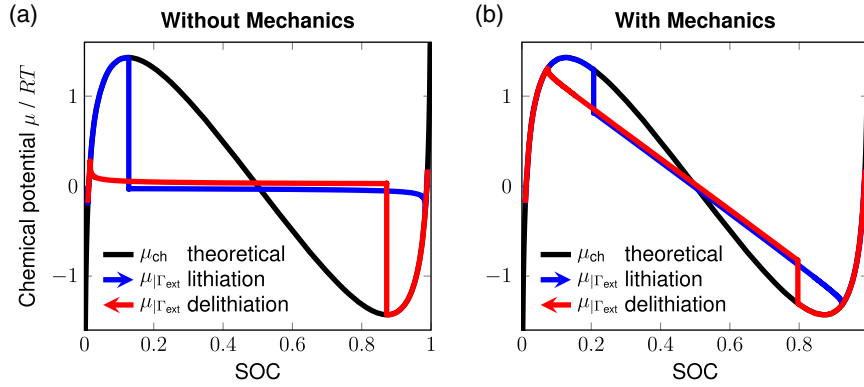


**Figure 8.** Hysteresis showing different chemical potentials at the particle surface ( $r = L_0$ ) during lithiation and delithiation versus the state of charge: a) without mechanics and b) with mechanics.

and blue, respectively, both with a quasi-static insertion rate of  $N_{\text{ext}} = 0.01$  C. In Figure 8a, we plot the hysteresis of the chemical potential without the mechanical effects. During lithiation, the chemical potential follows the black curve at low states of charge and then sharply drops to a negative value at the maximum of the chemical potential. During delithiation, the black and the red curve coincide for high states of charge and a sharp drop toward positive values occurs at the minimum of the chemical potential. In Figure 8b, we see the effects of mechanics on the chemical potential. The sharp decline of the chemical potential is smaller and shifted behind the maximum (lithiation) and minimum (delithiation). Moreover, the chemical potential decreases linearly over the state of charge instead of remaining constant.

To understand the hysteresis, we rely on the Gibbs stability criterion resulting from the second law of thermodynamics<sup>[55–57]</sup>

$$\frac{\partial \mu}{\partial c} > 0 \quad (40)$$

First, the particle lithiates to a SOC between the lithium poor phase and the lithium rich phase, which fulfills Equation (40). Once the chemical potential reaches the unstable region  $\partial \mu / \partial c < 0$ , the spinodal decomposition sets in and the particle spontaneously separates into a lithium poor and a lithium rich phase.<sup>[24]</sup> For delithiation, the process is inverted because  $-c$  instead of  $c$  increases over time. By including mechanics into this process, we extend the chemical potential by the elastic contributions

$$\mu_{\text{el}} = -\frac{\nu}{3\lambda_{\text{ch}}} \text{tr}(\mathbf{C}\mathbf{E}_{\text{el}}) \quad (41)$$

Deriving Equation (41) with respect to the concentration yields

$$\frac{\partial \mu_{\text{el}}}{\partial c} = \left( \frac{\nu}{3\lambda_{\text{ch}}^2} \right)^2 \text{tr}(\mathbf{C}(\mathbf{E}_{\text{el}} + 2\mathbf{C}_{\text{ch}})) \quad (42)$$

The derivative is positive, if the elastic deformation is smaller than the chemical deformation, which in our case is always fulfilled. Therefore, the Gibbs stability criterion (40) is valid for higher SOC, so that the spinodal decomposition is

shifted to higher SOC (lithiation) and lower SOC (delithiation). After the spinodal decomposition, the elastic part of the chemical potential, Equation (41), keeps rising according to Equation (42). Thus, we observe a linear decline of the chemical potential, so that the overall chemical potential remains constant.

### 4.3. Numerical Efficiency

So far we discussed the results of the numerical experiments from a physical point of view. In the rest of this section we discuss the numerical aspects of the solution algorithm presented in Section 3. We first validate our implemented solver numerically. Then we compare the efficiency of the adaptive algorithm to standard methods. Finally, we use our adaptive solver to the 2D geometry.

#### 4.3.1. Solver Validation

We validate our implementation by measuring the convergence of the numerical solution for spatial and temporal refinement, respectively. Because no exact solution is known for this problem, we consider the  $H^1$ -errors of the solution  $\gamma_h = [c_h, \mu_h, \mathbf{u}_h]^T$  to a reference solution  $\gamma_r$  at time  $t_f = 0.29$  (SOC = 0.3), when a phase transition is present

$$\begin{aligned} \text{ERR} := & \left( \left\| c_h(t_f, \cdot) - c_r(t_f, \cdot) \right\|_{H^1(\Omega)}^2 \right. \\ & + \left\| \mu_h(t_f, \cdot) - \mu_r(t_f, \cdot) \right\|_{H^1(\Omega)}^2 \\ & \left. + \left\| \mathbf{u}_h(t_f, \cdot) - \mathbf{u}_r(t_f, \cdot) \right\|_{H^1(\Omega)}^2 \right)^{1/2} \end{aligned} \quad (43)$$

The reference solution  $\gamma_r$  is assumed to approximate the unknown exact solution  $\gamma_{\text{ex}}$  more accurately than  $\gamma_h$  and is computed once with fourth-order finite elements and the tolerances  $\text{RelTol}_t = 10^{-8}$ ,  $\text{AbsTol}_t = 10^{-11}$  and  $\text{RelTol}_x = 10^{-20}$ ,  $\text{AbsTol}_x = 2 \times 10^{-11}$ .

For the experimental order of convergence of the spatial error, we fix an accurate time integration ( $\text{RelTol}_t = 10^{-7}$ ,  $\text{AbsTol}_t = 10^{-10}$ ) and compute the errors of the numerical solution on a series of successively uniformly refined meshes.

According to the theory of finite elements,<sup>[35]</sup> our implementation shows the optimal order of convergence for the finite element degrees one to four. A convergence analysis of the time integration with fixed spatial tolerances ( $\text{RelTol}_x = 10^{-20}$ ,  $\text{AbsTol}_x = 10^{-9}$ ) for fourth-order finite elements yields errors about  $10^{-8}$ . This validates our implementation.

### 4.3.2. Adaptivity

Next, we discuss the efficiency of our adaptive solution algorithm by analyzing the computational savings through spatial and temporal adaptivity for the simulation of lithium insertion as in Subsection 4.2.1.

**Spatial Adaptivity:** In **Figure 9a**, we illustrate the concentration profile in a phase separated state. Because the concentration profile is approximately constant except for the phase transition, a locally high resolution of the transition is advantageous. Accordingly, our algorithm distributes the DOFs adaptively considering the regularity estimator with respect to all solution variables ( $c_h$ ,  $\mu_h$ ,  $u_h$ ). The black circles in **Figure 9a** indicate the refinement level of the cells to reach a certain regularity tolerance. We observe that primarily the phase transition zone is resolved with additional DOFs. However, the mesh can also be locally refined in pure phases, for example, in the lithium rich

phase in **Figure 9a**, because we measure the regularity of all solution components.

Over time the phase transition migrates through the particle and the mesh is adapted. In **Figure 9b**, we plot the number of DOFs over time for different finite element orders. We again observe the three states of single- and two-phase diffusion. In particular, we see that higher order methods are beneficial for saving DOFs. This is due to better approximation properties of higher order curvatures in the solution profiles, as, for example, in the chemical potential profile.

We emphasize the computational savings by a comparison of the number of DOFs. For the adaptive fourth-order method, the minimal mesh width was  $2^{-9}$  and 1539 DOFs were distributed at maximum. In contrast, a linear finite element method would require, at least, a uniform mesh width  $2^{-11}$  and  $3 \times (2^{11} + 1) = 6147$  DOFs to distribute the same number of DOFs in the phase transition zone. We already reduced the maximum size of the linear systems by at least a factor of four. Thus, spatial adaptivity is one key for highly efficient solution algorithms.

**Temporal Adaptivity:** Another important key for the efficient solution is the adaptive time integration. In particular, we use an error controlled adaptive change in the time step size and the used order. Thereby, we benefit from higher order methods, which allow even larger time step sizes at the same error tolerance. In **Figure 10a**, we plot the time step size and the used order

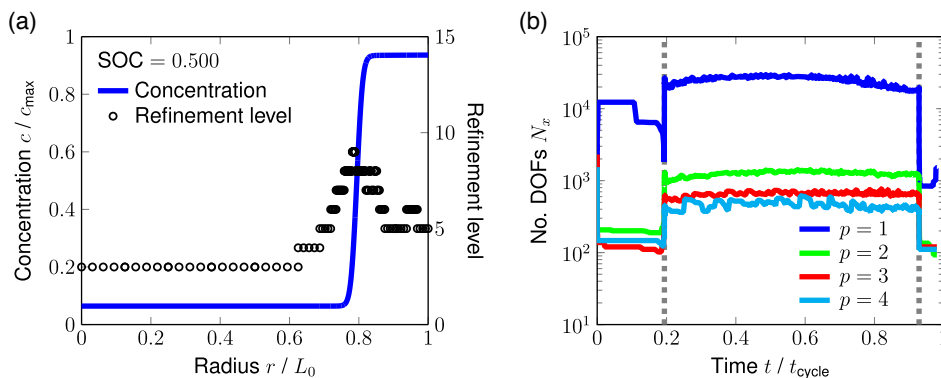


**Figure 9.** a) Concentration profile at SOC = 0.5 with adaptive refinement level and b) number of DOFs over time for different finite element method degrees.

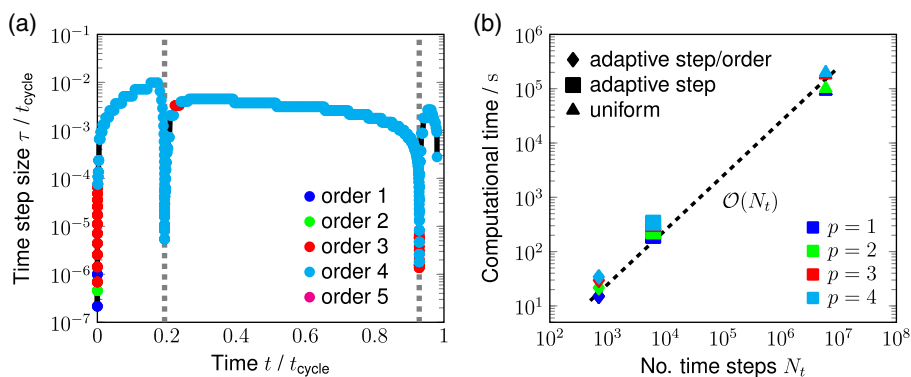


**Figure 10.** a) Time step size with used orders (markers) over time and b) computational wall time over the number of time steps for different time integration schemes and finite element orders.

over time. We identify the three regimes of single- and two-phase diffusion as before. The time step size varies over several orders of magnitude to capture the initiation and decay of the phase transition at the given tolerances. During two-phase diffusion up to the decay of the phase transition, we observe a decreasing time step size. This reflects the observation that in the radially symmetric case the phase transition migrates with increasing velocity toward the particle center. Thus, to keep the tolerances of the time integration, smaller time step sizes are necessary for the accelerating process.

The essential benefit from the temporal adaptivity is the use of large time step sizes during the two-phase diffusion. This advantage is particularly reflected in the number of time steps and the computational time. In Figure 10b, we plot the computational times for the whole solution process over the number of time steps for different strategies of time integration and finite element orders. To neglect the influence of spatial adaptivity, we used a uniform spatial discretization in all cases such that the phase transition is always resolved with at least ten unknowns ( $h = 2^{\lfloor \log_2(ps/10) \rfloor}$ ). In terms of computational time and number of time steps, the most efficient strategy is the fully adaptive algorithm changing the time step sizes and the orders adaptively (◆). Using the backward Euler method with an adaptive time step size (■), the computational times already increase by a factor of about ten. Last, we compare the number of time steps and the computational time for a constant step backward Euler method (▲). With the smallest adaptively chosen time step size from (■), the estimated number of time steps would increase by a factor of about 8000, compared with the fully adaptive strategy (◆). Hereby *estimated* means that we determined the computational time of one time step as average over 1000 steps and extrapolated this value to the total number of time steps.

#### 4.3.3. Spheroidal Electrode Particle

As proof of concept, we demonstrate the capabilities and efficiency of our adaptive solution algorithm at the 2D geometry described in Subsection 4.1. Even if the theory was derived assuming 3D geometries, the mathematical problem is still valid in lower dimensions. So neglecting any additional 3D symmetry we solve the model equations in Cartesian coordinates and postpone the further study of 2D and 3D particle geometries to future work.

In Figure 11, we see the concentration profile of the ellipse in the current configuration at three characteristic states during lithium insertion. In accordance with Santoki et al.,<sup>[58]</sup> we observe in Figure 11a the initiation of the phase separation at surfaces with

high curvature. The insertion process is then followed by the migration of two traveling fronts until they merge in the particle center. During lithiation we observe that unstable nucleation can occur forming small domains of lithium rich phases. However, these domains vanish after a short time and only the two stable fronts remain.

In addition, Figure 11 visualizes the adaptive mesh. We see clearly that the mesh is only resolved at the phase transition, which migrates through the particle's domain over time. In the lithium poor and rich bulk phases, a coarser resolution can be applied. During the simulation we distributed between  $2.5 \times 10^3$  and  $1.7 \times 10^5$  DOFs. In contrast, a uniform mesh with the same maximum level as in the adaptive case would have approximately  $2.1 \times 10^7$  DOFs. Thus, we reduced the number of DOFs by a factor of at least  $10^2$  and solved this example in less than 5 h on the cluster specified in Section 4.1.

## 5. Summary and Conclusion

Summing up, we have developed a thermodynamically consistent phase-field model coupling Cahn–Hilliard-type phase separation and finite deformations during the lithiation of electrode particles in lithium-ion batteries. In addition, we have presented our implemented space and time adaptive, higher order finite element solver for the numerical simulation of the resulting model equations. For the example of lithium iron phosphate as electrode material, we have performed several simulations to investigate physical and numerical aspects of the model and the solver.

A comparison of our simulation results with the literature<sup>[11,17,21–26,33]</sup> showed excellent qualitative accordance. In particular, we revealed that the interfacial energy coefficient  $\kappa$  is critical to determine the maximum occurring stress inside an electrode particle. However, 3D phase-field simulations, as, for example, in Refs. [26,32,33], often rely on larger values of  $\kappa$  than radially symmetric, 1D simulations<sup>[23–25]</sup> to reduce the computational costs, eventually leading to underestimated stress magnitudes.

Comparing the computational time with our problem-tailored solution algorithm to a standard implementation based on a constant step size backward Euler scheme together with a linear finite element method implementation revealed an estimated speedup of about 8000. We achieve this speedup, by using a space and time adaptive, higher order finite element solver. The time adaptivity greatly decreases the simulation time by selectively resolving the emergence and decay of the phase

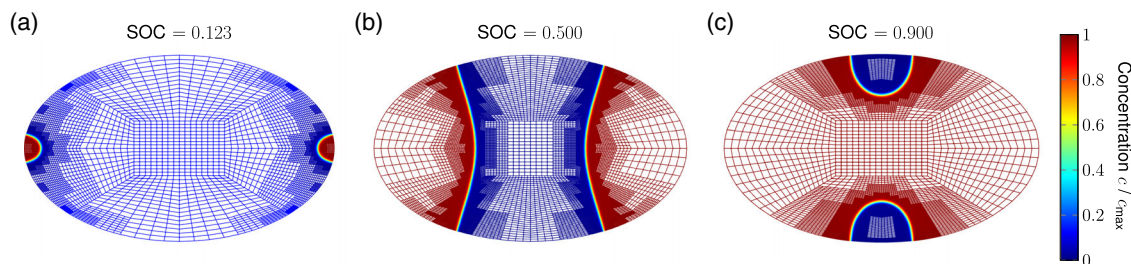


**Figure 11.** Concentration profile in a 2D ellipsoidal particle domain at different SOC levels with adaptive meshes.

separation. The spatial adaptivity reduces the computational costs by only locally refining the mesh at the phase transition. The advantages of adaptive methods are especially beneficial for the 2D example of a generic spheroidal shaped electrode particle. With this analysis we have demonstrated that adaptive methods are a powerful tool for efficient simulations.

Future works will rely on this numerical efficiency and extend the implementation to three dimensions. This paves the way to analyze the anisotropy of typical cathode particles as well as inhomogeneous boundary conditions, e.g., constrained expansion and nonuniform charging. Furthermore, our implementation enables the simulation of almost sharp interfaces. By implementing an additional model for particle fracture, it will, thus, be possible to resolve mechanical degradation in unprecedented speed and accuracy. In addition, we can implement our fast single particle model in multiscale battery simulations to increase computational efficiency.

## Acknowledgements

The authors acknowledge computational time on the cluster *Horst* and, in particular, thank S. Simonis and J. E. Marquardt for helpful advices concerning the cluster. G.F.C. and L.v.K. acknowledge financial support by the German Research Foundation (DFG) through RTG 2218 SiMET – Simulation of mechano-electro-thermal processes in lithium-ion batteries, project number 281041241.

Open access funding enabled and organized by Projekt DEAL.

## Conflict of Interest

The authors declare no conflict of interest.

## Data Availability Statement

Research data are not shared.

## Keywords

finite element method, lithium-ion batteries, mechanics, numerical simulation, phase-field models

Received: September 22, 2020

Revised: February 10, 2021

Published online: May 5, 2021

- 
- [1] M. Armand, J.-M. Tarascon, *Nature* **2008**, 451, 7179.  
 [2] R. Xu, K. Zhao, *J. Electrochem. En. Conv. Stor.* **2016**, 13, 030803.  
 [3] M. T. McDowell, I. Ryu, S. W. Lee, C. Wang, W. D. Nix, Y. Cui, *Adv. Mater.* **2012**, 24, 6034.  
 [4] J. Christensen, J. Newman, *J. Solid State Electrochem.* **2006**, 10, 293.  
 [5] H. Yang, W. Liang, X. Guo, C. M. Wang, S. Zhang, *Extreme Mech. Lett.* **2015**, 2, 1.  
 [6] B. W. Sheldon, S. K. Soni, X. Xiao, Y. Qi, *Electrochem. Solid-State Lett.* **2012**, 15, A9.  
 [7] R. Xu, L. Scalco De Vasconcelos, K. Zhao, *J. Mater. Res.* **2016**, 31, 2715.  
 [8] H. Tian, F. Xin, X. Wang, W. He, W. Han, *J. Materiomics* **2015**, 1, 153.  
 [9] A. Van Der Ven, C. Marianetti, D. Morgan, G. Ceder, *Solid State Ion.* **2000**, 135, 21.  
 [10] A. Yamada, H. Koizumi, S. I. Nishimura, N. Sonoyama, R. Kanno, M. Yonemura, T. Nakamura, Y. O. Kobayashi, *Nat. Mater.* **2006**, 5, 357.  
 [11] A.-C. Walk, M. Huttin, M. Kamlah, *Eur. J. Mech. A Solids* **2014**, 48, 74.  
 [12] A. Van Der Ven, J. Bhattacharya, A. A. Belak, *Acc. Chem. Res.* **2013**, 46, 1216.  
 [13] C. Delmas, M. Maccario, L. Croguennec, F. Le Cras, F. Weill, *Nat. Mater.* **2008**, 7, 665.  
 [14] Y. Zhao, P. Stein, Y. Bai, M. Al-Siraj, Y. Yang, B.-X. Xu, *J. Power Sources* **2019**, 413, 259.  
 [15] J. W. Cahn, J. E. Hilliard, *J. Chem. Phys.* **1958**, 28, 258.  
 [16] J. W. Cahn, *Acta Metall.* **1961**, 9, 795.  
 [17] L. Chen, F. Fan, L. Hong, J. Chen, Y. Z. Ji, S. L. Zhang, T. Zhu, L. Q. Chen, *J. Electrochem. Soc.* **2014**, 161, F3164.  
 [18] E. Meca, A. Münch, B. Wagner, *Proc. R. Soc. A* **2016**, 472, 20160093.  
 [19] E. Meca, A. Münch, B. Wagner, *Eur. J. Appl. Math.* **2018**, 29, 118.  
 [20] K. Zhang, Y. Li, F. Wang, B. Zheng, F. Yang, *J. Phys. D: Appl. Phys.* **2019**, 52, 145501.  
 [21] M. Huttin, M. Kamlah, *Appl. Phys. Lett.* **2012**, 101, 133902.  
 [22] T. Zhang, M. Kamlah, *Contin. Mech. Thermodyn.* **2018**, 30, 553.  
 [23] T. Zhang, M. Kamlah, *Electrochim. Acta* **2019**, 298, 31.  
 [24] T. Zhang, M. Kamlah, *J. Electrochem. Soc.* **2018**, 165, A1997.  
 [25] T. Zhang, M. Kamlah, *J. Electrochem. Soc.* **2020**, 167, 020508.  
 [26] C. V. Di Leo, E. Rejovitzky, L. Anand, *J. Mech. Phys. Solids* **2014**, 70, 1.  
 [27] D. A. Cogswell, M. Z. Bazant, *ACS Nano* **2012**, 6, 2215.  
 [28] N. Nadkarni, E. Rejovitzky, D. Fraggedakis, C. V. Di Leo, R. B. Smith, P. Bai, M. Z. Bazant, *Phys. Rev. Materials* **2018**, 2, 085406.  
 [29] M. Tang, J. F. Belak, M. R. Dorr, *J. Phys. Chem. C* **2011**, 115, 4922.  
 [30] M. J. Welland, D. Karpeyev, D. T. O'Connor, O. Heinonen, *ACS Nano* **2015**, 9, 9757.  
 [31] M. Huttin, Ph.D. Thesis, Karlsruhe Institute of Technology (KIT) **2014**.  
 [32] Y. Zhao, P. Stein, B.-X. Xu, *Comput. Methods Appl. Mech. Engrg.* **2015**, 297, 325.  
 [33] Y. Zhao, B.-X. Xu, P. Stein, D. Gross, *Comput. Methods Appl. Mech. Engrg.* **2016**, 312, 428.  
 [34] B.-X. Xu, Y. Zhao, P. Stein, *GAMM-Mitt.* **2016**, 39, 92.  
 [35] D. Braess, *Finite Elements*, 3rd edn, Cambridge University Press, Cambridge **2007**.  
 [36] G. A. Holzapfel, *Nonlinear Solid Mechanics*, John Wiley & Sons, Ltd., Chichester, **2000**.  
 [37] M. Schammer, B. Horstmann, A. Latz, *J. Electrochem. Soc.* **2021**, 168, 026511.  
 [38] B. C. Han, A. Van Der Ven, D. Morgan, G. Ceder, *Electrochim. Acta* **2004**, 49, 4691.  
 [39] Y. Zeng, M. Z. Bazant, *SIAM J. Appl. Math.* **2014**, 74, 980.  
 [40] V. Hoffmann, G. Pulletikurthi, T. Carstens, A. Lahiri, A. Borodin, M. Schammer, B. Horstmann, A. Latz, F. Endres, *Phys. Chem. Chem. Phys.* **2018**, 20, 4760.  
 [41] G. F. Castelli, W. Dörfler, *Numerical Mathematics and Advanced Applications ENUMATH 2019*, Vol. 139, (Eds: F. J. Vermolen, C. Vuik) Springer **2021**.  
 [42] The MathWorks Inc., MATLAB, <http://www.mathworks.com>.  
 [43] L. F. Shampine, M. W. Reichelt, *SIAM J. Sci. Comput.* **1997**, 18, 1.  
 [44] L. F. Shampine, M. W. Reichelt, J. A. Kierzenka, *SIAM Rev.* **1999**, 41, 538.  
 [45] L. F. Shampine, I. Gladwell, S. Thompson, *Solving ODEs With MATLAB*, Cambridge University Press, Cambridge, **2003**.  
 [46] G. F. Castelli, Ph.D. Thesis, Karlsruhe Institute of Technology (KIT) **2021**, (Unpublished).

- [47] M. Ainsworth, J. T. Oden, in *Pure and Applied Mathematics*. John Wiley & Sons, Inc., New York, NY, **2000**.
- [48] L. Bañas, R. Nürnberg, *J. Comput. Appl. Math.* **2008**, 218, 2.
- [49] L. Hong, L. Li, Y.-K. Chen-Wiegart, J. Wang, K. Xiang, L. Gan, W. Li, F. Meng, F. Wang, J. Wang, Y.-M. Chiang, S. Jin, M. Tang, *Nat. Commun.* **2017**, 8, 1194.
- [50] Y. Qi, L. G. Hector, C. James, K. J. Kim, *J. Electrochem. Soc.* **2014**, 161, F3010.
- [51] T. Maxisch, G. Ceder, *Phys. Rev. B* **2006**, 73, 174112.
- [52] W. Bangerth, R. Hartmann, G. Kanschat, *ACM Trans. Math. Softw.* **2007**, 33, 24/1.
- [53] T. A. Davis, *ACM Trans. Math. Softw.* **2004**, 30, 196.
- [54] L. Wu, V. D. Andrade, X. Xiao, J. Zhang, *ASME J. Electrochem. En. Conv. Stor.* **2019**, 16, 041006.
- [55] J. W. Gibbs, *The Collected Works of J. Willard Gibbs: In Two Volumes*, Longmans, Green and Co., New York, NY **1928**.
- [56] B. Horstmann, B. Gallant, R. Mitchell, W. G. Bessler, Y. Shao-Horn, M. Z. Bazant, *J. Phys. Chem. Lett.* **2013**, 4, 4217.
- [57] M. Z. Bazant, *Faraday Discuss.* **2017**, 199, 423.
- [58] J. Santoki, D. Schneider, M. Selzer, F. Wang, M. Kamlah, B. Nestler, *Modell. Simul. Mater. Sci. Eng.* **2018**, 26, 065013.